Role of nuclear spin in photoionization: Hyperfine-resolved photoionization of Xe and multichannel quantum defect theory analysis

H. J. Wörner, M. Grütter, E. Vliegen, and F. Merkt*
Laboratorium für Physikalische Chemie, ETH Zürich, CH-8093 Zurich, Switzerland
(Received 2 December 2004; published 12 May 2005)

High-resolution photoionization spectra following single-photon excitation from the $^1S_0$ ground state have been recorded for the seven most abundant isotopes of xenon in the range between the first $^2P_{3/2}$ and the second $^2P_{1/2}$ ionization thresholds. Accurate values for the ionization energies $V_{\mathrm{ion}}(^2P_{1/2})$ and isotope shifts have been derived enabling the determination of the spin-orbit splitting in Xe^+ with an unprecedented accuracy. The narrow bandwidth of the vuv laser (250 MHz) has enabled the resolution of the hyperfine structure of the autoionizing ns' series of ^{129}Xe and ^{131}Xe in the range of principal quantum number $n=30$–150. Multichannel quantum defect theory (MQDT) has been extended to treat the hyperfine structure of autoionizing Rydberg series and to derive the hyperfine structure of the $^2P_{1/2}$ state of the singly charged ion. The MQDT analysis demonstrates the possibility of producing ions in selected hyperfine states by photoionization and enables the characterization of the combined effects of the spin-orbit and hyperfine autoionization.

DOI: 10.1103/PhysRevA.71.052504 PACS number(s): 32.10.Fn, 32.80.Rm, 32.30.Jc, 34.60.+z

I. INTRODUCTION

The role of nuclear spin in chemical reactions is well understood in terms of symmetry selection rules [1]. In molecular photoionization, these imply the conservation of nuclear spin symmetry [2,3]. Further dynamical effects of the nuclear spins in the photoionization of atoms and molecules have so far received little attention because the ionization channels associated with distinct hyperfine levels of the ions have not been resolved. The progress in high-resolution laser spectroscopy over the past years has been such that very high Rydberg states (up to $n=200$ and beyond) can now be resolved even in the extreme ultraviolet [4], where a resolution of about 250 MHz has been achieved [5]. At this resolution, the hyperfine structure of Rydberg states can be observed and represents a valuable source of information on the hyperfine levels of the ion to which the Rydberg electron is attached and on the photoionization dynamics. In parallel to the experimental efforts, multichannel quantum defect theory (MQDT) [6–9] has been extended to treat the hyperfine structure of bound atomic and molecular Rydberg states [10–12] and has provided a theoretical framework to determine ionic hyperfine structures from extrapolation of Rydberg series. This method has been successfully applied to derive the hyperfine structure of the ground state of $^{83}Kr^+$ [11] and ortho-H_2^+ [12]. The desire to understand the role of nuclear spin in photoionization and to extend the experimental and theoretical investigation of the hyperfine structure of bound Rydberg states to autoionizing states has motivated the present combined experimental and theoretical analysis of the Rydberg spectrum of Xe.

In atomic and molecular physics the process of autoionization is classified as electronic, vibrational, spin-orbit, or rotational according to the type of energy that is transferred from the ionic core to the Rydberg electron (rather than according to the type of interaction responsible for the ionization) [13,14]. This nomenclature implies the name "hyperfine autoionization" for the autoionization process by which the hyperfine energy of the core is transferred to cause ionization. An important goal of the present work was to study this process of hyperfine autoionization on the basis of hyperfine resolved spectroscopic data. Figure 1 contrasts spin-orbit autoionization encountered in the $I=0$ xenon isotopes and which leads to the well-known Beutler-Fano profiles [15,16] of the autoionization region of the xenon spectrum between the $^2P_{3/2}$ and $^2P_{1/2}$ ionization limits [Fig. 1(b)] with the qualitatively different situation that arises in the isotopes of xenon with $I\neq 0$ [^{129}Xe, $I=1/2$, see Fig. 1(d), and ^{131}Xe, $I=3/2$].

In the $I=0$ isotopes, autoionization results in a change of spin-orbit state of the ionic core, whereas in the $I\neq 0$ isotopes, the autoionization may involve either a change of spin-orbit core state, hyperfine core state, or both. The autoionization region around $n=68$ depicted in Figs. 1(b) and 1(d), as obtained in the present study, reveals a completely different spectral structure for the $I\neq 0$ isotopes. To our knowledge, this autoionization structure of the $I\neq 0$ isotopes of xenon has not been observed or discussed in the literature despite the fact that the spectral resolution required for its observation would have been available.

In particular we address here the following questions: (i) Is pure hyperfine autoionization, i.e., a process in which the ionization is solely accompanied by a change of the hyperfine state of the ion core, allowed? (ii) What are the propensity rules $(\Delta J^+, \Delta F^+)$ describing the energy flow between core and Rydberg electron in the autoionization region of the $I\neq 0$ isotopes of Xe? (iii) Can such propensities, if they exist, be exploited to prepare ions in selected hyperfine states, with possible applications in ion-trap loading [17] and quantum computing [18]?

To answer these questions, we combine high-resolution spectroscopy and MQDT to describe the influence of the nuclear spin on the structure and dynamics of the states embedded in the autoionization continuum and to predict the

*Author to whom correspondence should be addressed.

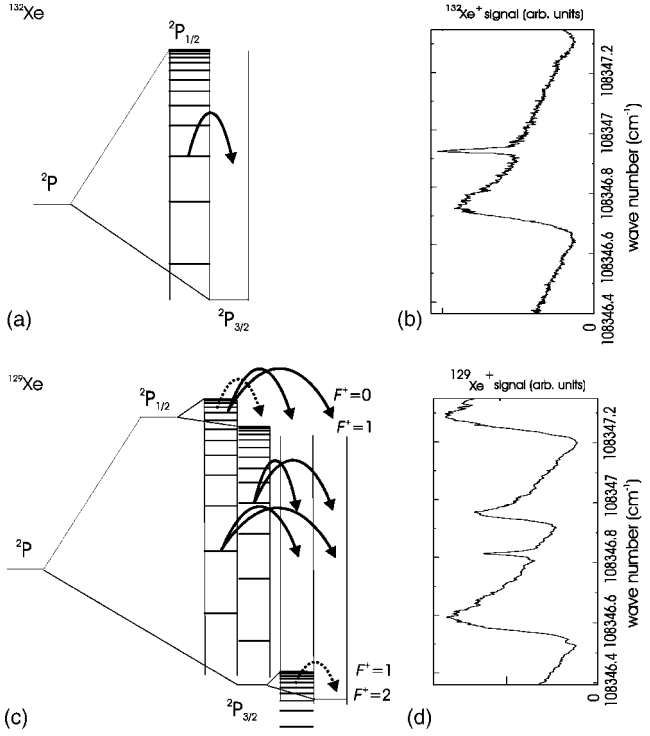

FIG. 1. Schematic energy-level diagram of the autoionizing Rydberg series of ^{132}Xe (a) and ^{129}Xe (c). The full arrows represent the process of spin-orbit autoionization that leads in both cases to an ion in the $^2P_{3/2}$ state. The dotted arrows in panel (c) represent hyperfine autoionization processes. Panels (b) and (d) show the observed photoionization spectra of ^{132}Xe (b) and ^{129}Xe (d) in the region around $n=68$. Panel (b) shows the well-known Beutler-Fano profiles, whereas the spectrum in panel (d) is qualitatively different, because of additional interactions with the nuclear spin ($I=1/2$ of ^{129}Xe).

branching ratios for ionization into the fine and hyperfine structure components accessible at a given photoionization energy. The MQDT model also enables a discussion and a characterization of the mechanism responsible for the process of hyperfine autoionization.

The autoionization resonances of xenon between its first ($^2P_{3/2}$) and second ($^2P_{1/2}$) ionization thresholds have been observed by Beutler [15] and understood in the light of a theoretical contribution by Fano [16]. Since then, this region of the xenon spectrum has been thoroughly studied both experimentally [19–22] and theoretically [6,23]. The *ab initio* prediction of the line shapes of the lowest autoionizing resonances remains a challenge up to present day and continues to stimulate theoretical efforts [24,25]. The experimental methods include energy-loss spectroscopy [19], single-photon [20–22], and three-photon spectroscopy [26] of the odd parity ($J=1$ and 3) series and two-photon excitation of s series with $J=0$, 1 and d series with $J=1$, 2, 3 from metastable levels [27]. MQDT analyses have been performed for the bound levels and the first autoionization resonances (odd-parity,
$J=1$) [6,19], for the bound d and autoionizing s' levels with $J=0$ [28], and for the odd-parity bound levels with $J=0$, 2, 3 [29].

The hyperfine structure and isotope shifts of bound levels of xenon have been studied to characterize the multipole moments of the hyperfine interaction and the nuclear structure [30–33]. The hyperfine structure of several excited states of Xe^+ has also been studied experimentally (see, e.g., Ref. [34] and references therein) and theoretically [35] but, to our knowledge, the hyperfine structure of the two spin-orbit components of its ^2P ground state has not been determined.

Xenon represents an ideal model system for the investigation of the hyperfine structure in the autoionization continuum because (i) the magnetic dipole hyperfine constants $A_{1/2}$ of the $^2P_{1/2}$ state of $^{129}Xe^+$ and $^{131}Xe^+$ are large, (ii) the spectrum of the isotopes with zero nuclear spin has been analyzed in detail by MQDT, and (iii) two isotopes with different nuclear spin are observable in a single experiment. In addition, a measurement of the hyperfine structure of the $^2P_{1/2}$ level can be used to derive an improved value of the spin-orbit splitting in the ^2P ground state of Xe^+.

This paper is structured as follows: Sec. II provides a short description of the experimental procedure. The MQDT formalism describing the hyperfine structure of bound Rydberg states is briefly reviewed and extended to describe the autoionizing region of the spectrum in Sec. III. Section IV provides an analysis of the spectra of the isotopes with zero nuclear spin, which enabled the derivation of an accurate value of the spin-orbit splitting in Xe^+. It also summarizes the analysis of the hyperfine structure in the spectra of ^{129}Xe and ^{131}Xe from which values for the magnetic dipole hyperfine constants $A_{1/2}$ for $^{129}Xe^+$ and $^{131}Xe^+$ could be derived. In Sec. V, the results are discussed and predictions are made concerning the production of ions in selected hyperfine states by photoionization. Finally, the mechanism underlying the phenomenon of hyperfine autoionization is discussed and shown to be analogous to that responsible for spin-orbit autoionization.

II. EXPERIMENT

The spectra have been recorded using a narrow bandwidth (250 MHz) tunable vuv laser system coupled to a photoion/photoelectron time-of-flight (TOF) mass spectrometer. The main aspects of our experimental procedure have been described in detail earlier [5,36] and are only briefly summarized here.

vuv radiation is generated by two-photon resonance-enhanced sum-frequency mixing ($\nu_{vuv}=2\nu_1+\nu_2$) in Kr using the $(4p)^5 5p[1/2]_0 \leftarrow (4p)^6 {}^1S_0$ two-photon resonance at $2\tilde{\nu}_1 = 94\,092.9\ \mathrm{cm}^{-1}$. To achieve a near-Fourier-transform-limited vuv bandwidth, two pulsed-amplified cw ring dye lasers are used as input beams to the nonlinear frequency up-conversion process. The vuv radiation is separated from the fundamental beams in a vacuum monochromator. The separation is achieved by a toroidal dispersion grating which also recollimates the diverging vuv beam and redirects it towards a photoexcitation-photoionization chamber equipped with a linear TOF mass spectrometer. The vuv wave number is calibrated to an absolute accuracy of 0.016 cm^{-1} following the procedure described in Ref. [36] which involves the stabilization of the wave number of the first laser. The wave

number of the second laser is calibrated by recording absorption spectra of molecular iodine in an oven heated to 600 °C and comparing them to spectra simulated with the program IODINESPEC [37].

Xenon gas (Pangas, spectroscopic grade purity) is used without further purification and is introduced into the spectrometer in a pulsed skimmed supersonic expansion. The xenon gas jet is crossed at a right angle by the vuv laser beam in the middle of an array of resistively coupled cylindrical extraction plates. The photoexcitation region and the TOF mass spectrometer are surrounded by a double layer of Mu-metal shielding. Under the experimental conditions used to record the photoionization spectra of the high Rydberg states of xenon, dc and ac Stark shifts are negligible for the Rydberg states with principal quantum number between 30 and 150 used in the MQDT analysis.

Spectra of the autoionizing Rydberg states located below the $^2P_{1/2}$ ionization threshold were recorded by monitoring the photoionization yield as a function of the vuv wave number. The ions were extracted towards a microchannel plate detector located at the end of the TOF tube by a pulsed electric field of 88 V/cm amplitude and 1 μs duration which was applied 1 μs after the vuv laser pulse so that photoexcitation could take place under field-free conditions. Spectra of the different isotopes were obtained by placing temporal gates at the corresponding positions in the TOF spectrum. Photoionization spectra with a satisfactory signal-to-noise ratio could be obtained for the isotopes $^{128\text{-}132,134,136}$Xe but not for ^{124}Xe and ^{126}Xe. The wave-number range covered in these experiments extends from 108 275 cm^{-1} to 108 371 cm^{-1}. A low efficiency in the resonance-enhanced sum-frequency mixing prevented the recording of spectra in the region between 108 315 cm^{-1} and 108 340 cm^{-1}.

III. MQDT OF THE HYPERFINE STRUCTURE OF AUTOIONIZING RYDBERG STATES OF XENON

In a previous publication, an MQDT model was developed to analyze the hyperfine structure of bound Rydberg states of the rare-gas atoms and used to quantitatively account for the Rydberg spectrum of ^{83}Kr below the $^2P_{3/2}$ ionization limit and determine the hyperfine structure of ^{83}Kr$^+$ in its $^2P_{3/2}$ ground state [11]. In the following, this formalism is briefly reviewed and extended to treat the hyperfine structure of autoionizing Rydberg states of the rare-gas atoms.

MQDT relies on a partitioning of space into two regions. At short electron-core distances, the so-called close-coupling region, the interactions between the ion core and the Rydberg electron are dominated by electrostatic (including exchange) interactions. The following angular momentum coupling hierarchy provides an adequate description of the close-coupling eigenchannels [6]:

$$\vec{L}^+ + \vec{\ell} = \vec{L};\ \vec{S}^+ + \vec{s} = \vec{S};\ \vec{L} + \vec{S} = \vec{J}, \vec{J} + \vec{I} = \vec{F}, \tag{1}$$

where $\vec{L}^+$ and $\vec{S}^+$ represent the orbital and spin angular momenta of the ionic core, $\vec{\ell}$ and $\vec{s}$ the corresponding angular momenta of the Rydberg electron, and $\vec{I}$ the nuclear spin. The parameters characterizing the interactions in the close-coupling region are the eigenquantum defects μ_α which are assumed to be unaffected by the hyperfine interactions and can thus be taken from an analysis of the $I=0$ isotopes [11]. The choice of this coupling scheme for the description of the close-coupling channels is equivalent to a neglect of the spin-orbit and hyperfine interactions in the core. This choice is further discussed in Sec. V.

At large electron-core distances, the electron interacts only weakly with the core. In this region, the dissociation channels can be described by the following angular momentum coupling scheme:

$$\vec{L}^+ + \vec{S}^+ = \vec{J}^+,\ \vec{J}^+ + \vec{I} = \vec{F}^+;\ \vec{\ell} + \vec{s} = \vec{j},\ \vec{F}^+ + \vec{j} = \vec{F}, \tag{2}$$

where $\vec{J}^+$ and $\vec{F}^+$ represent the electronic and total angular momenta of the ionic core, respectively. The dominant interaction in the ionic core is the spin-orbit coupling which leads to an energy splitting between the $^2P_{3/2}$ and $^2P_{1/2}$ levels, that is several orders of magnitude larger than the splittings induced by the hyperfine interactions. Under the assumption that the mixing of the $^2P_{3/2}$ and $^2P_{1/2}$ spin-orbit components of the ion by the hyperfine interactions is negligible, the hyperfine structure of the two spin-orbit components can be treated separately and expressed as a function of the magnetic dipole and electric quadrupole hyperfine coupling constants A_{J^+} and B_{J^+} [38] ($B_{J^+=1/2}=0$ for the $^2P_{1/2}$ spin-orbit level):

$$\tilde{\nu}(J^+,F^+) = \tilde{\nu}_{J^+} + A_{J^+}\frac{C}{2} + B_{J^+}\frac{\frac{3}{4}C(C+1) - I(I+1)J^+(J^+ + 1)}{2I(2I-1)J^+(2J^+ - 1)}, \tag{3}$$

where

$$C = F^+(F^+ + 1) - I(I+1) - J^+(J^+ + 1). \tag{4}$$

In Eq. (3), $\tilde{\nu}_{J^+}$ represents the wave number of the photoionization transition to the center of gravity of the hyperfine structure for each of the two spin-orbit $^2P_{J^+}$ components ($J^+=1/2,\ 3/2$). The dissociation channels are hence characterized by a pair of intermediate quantum numbers J^+ and F^+ designating each ionization threshold.

The parameter characterizing a closed dissociation channel i built on an ionic core with intermediate quantum numbers J^+ and F^+ is the effective quantum number

$$\nu_i = \sqrt{\frac{R_M}{\tilde{\nu}_{J^+F^+} - \tilde{\nu}}}. \tag{5}$$

The analytical frame transformation

$$U_{i\alpha} = \langle LSJF | J^+F^+jF \rangle \tag{6}$$

between the bases of the $LSJF$-coupled eigenchannels and the J^+F^+jF-coupled dissociation channels was derived using angular momentum algebra [see Eq. (17) of Ref. [11]].

If the total energy of the system lies below the lowest ionization energy, all channels are closed and the positions of bound Rydberg states are obtained by requiring the wave functions to vanish at an infinite ion-electron distance r. This condition translates into the equation

$$\sum_{\alpha} U_{i\alpha}\sin[\pi(\mu_\alpha + \nu_i)]A_\alpha = 0, \tag{7}$$

where the A_α are the expansion coefficients of the radial part of the Rydberg electron wave function in the basis of the close-coupling eigenchannels. This equation has nontrivial solutions when

$$\det|U_{i\alpha}\sin[\pi(\mu_\alpha + \nu_i)]| = 0. \tag{8}$$

If the total energy lies between the lowest and the highest ionization energy included in the MQDT model, some dissociation channels are closed. The ensemble of closed channels is denoted Q whereas the ensemble of open channels is labeled P. In this region of the spectrum, the boundary condition requires that the closed-channel wave functions remain finite for $r \to \infty$ and that the open-channel wave functions behave at large r as collision eigenfunctions of the open channels, labeled ρ, with a phase shift τ_ρ. The following set of equations is obtained from these boundary conditions:

$$\sum_{\alpha} U_{i\alpha}\sin[\pi(\mu_\alpha + \nu_i)]A_\alpha = 0 \text{ for } i \in Q, \tag{9}$$

$$\sum_{\alpha} U_{i\alpha}\sin[\pi(-\tau_\rho + \nu_i)]A_\alpha = 0 \text{ for } i \in P, \tag{10}$$

and the corresponding compatibility condition is solved in the form of a generalized eigenvalue problem [39].

For each value of the total energy in the autoionization region there are as many solutions τ_ρ and associated vectors of expansion coefficients $\mathbf{A}^\rho$ as open channels. These coefficients are obtained in a single step by solving the equation

$$\mathbf{\Gamma A}^\rho = \tan(\pi\tau_\rho)\mathbf{\Lambda A}^\rho, \tag{11}$$

where

$$\Gamma_{i\alpha} = \begin{cases} U_{i\alpha}\sin[\pi(\nu_i + \mu_\alpha)] & \text{for } i \in Q \\ U_{i\alpha}\sin(\pi\mu_\alpha) & \text{for } i \in P, \end{cases} \tag{12}$$

$$\Lambda_{i\alpha} = \begin{cases} 0 & \text{for } i \in Q \\ U_{i\alpha}\cos(\pi\mu_\alpha) & \text{for } i \in P. \end{cases} \tag{13}$$

The single-photon excitation to a dissociation channel i is described as the excitation into eigenchannels α, followed by an expansion in a basis of collision eigenfunctions ρ, which are projected onto the dissociation channels i. The partial photoionization cross sections are obtained as a coherent sum over contributions from the collision eigenfunctions ρ of all open channels. Each contribution is the product of an excitation amplitude, which depends on the close-coupling eigenchannel character A_α^ρ of ρ, a phase factor which contains the Coulomb phase and the phase shift of the collision function τ_ρ, and the projection $\langle i|\rho\rangle$ of the collision eigenfunction ρ onto the dissociation channel i. The partial photoionization cross section into a particular channel thus depends on (i) the importance of excitable close-coupling eigenchannel in the collision function, (ii) the strength of the channel coupling given by $\langle i|\rho\rangle$, and (iii) the collision phase shifts τ_ρ. The partial photoionization cross section for the generation of an ion in the state labeled by the quantum numbers J^+ and F^+ is given by [40]

$$\sigma_{J^+F^+} \propto \omega \sum_F W_F \sum_{i \in P_{J^+F^+}} |D(i,F)|^2, \tag{14}$$

where ω is the energy of the incident photon and $D(i,F)$ is the reduced dipole matrix element for the photoionization from the ground state. W_F is a weighting factor that accounts for the multiplicity of the levels accessed by photoexcitation from the $^1S_0$ ground state [41],

$$W_F = \frac{2F+1}{2I+1}. \tag{15}$$

The total photoionization cross section is given by

$$\sigma_{\text{tot}} = \sum_{J^+F^+} \sigma_{J^+F^+}. \tag{16}$$

The reduced dipole matrix element can be expressed as a function of the MQDT parameters [40],

$$D(i,F) = \sum_\rho e^{i(\sigma_i - \pi\ell_i/2)}\langle i|\rho\rangle e^{i\pi\tau_\rho} \sum_\alpha \frac{A_\alpha^\rho D_\alpha}{N_\rho}, \tag{17}$$

where $\sigma_i, \langle i|\rho\rangle$ and N_ρ are defined as

$$\sigma_i = \arg\left[\Gamma\left(\ell_i + 1 - i\sqrt{\frac{R_M}{\tilde{\nu} - \tilde{\nu}_i}}\right)\right], \tag{18}$$

$$\langle i|\rho\rangle = \frac{\sum_\alpha U_{i\alpha}\cos[\pi(-\tau_\rho + \mu_\alpha)]A_\alpha^\rho}{N_\rho}, \tag{19}$$

$$N_\rho^2 = \sum_{i \in P}\left(\sum_\alpha U_{i\alpha}\cos[\pi(-\tau_\rho + \mu_\alpha)]A_\alpha^\rho\right)^2. \tag{20}$$

The electric dipole transition amplitudes D_α were taken from Ref. [6] to be $D_{(p^5d)^1P_1}/D_{(p^5s)^1P_1} = 5$ and $D_\alpha = 0$ for all other channels, independently of the value of F.

IV. RESULTS

A. Photoionization spectra of the xenon isotopes with zero nuclear spin

The photoionization spectra of the xenon isotopes with zero nuclear spin are characterized by two series $ns'[1/2]_1$ and $nd'[3/2]_1$ converging to the $^2P_{1/2}$ state of the ion. These spectra are usually analyzed with the effective two-channel formalism derived from MQDT [42], which represents the photoionization spectrum by the expression

$$\sigma = \sigma_{\text{as}}\frac{(\epsilon_{\text{s}} + q_{\text{s}})^2}{(\epsilon_{\text{s}}^2 + 1)} + \sigma_{\text{ad}}\frac{(\epsilon_{\text{d}} + q_{\text{d}})^2}{(\epsilon_{\text{d}}^2 + 1)} + \sigma_{\text{b}}, \tag{21}$$

where

TABLE I. $^2P_{1/2}$ ionization energy $E_{\rm ion}(^2P_{1/2})$, quantum defects, and line-shape parameters for d' resonances obtained from numerical fits of Eq. (21) to the photoionization spectrum of ^{132}Xe in the ranges $\nu_{1/2}\approx 33$–42 and 65–92.

	This work	Literature
$E_{\rm ion}(^2P_{1/2})/(hc\ {\rm cm}^{-1})$	108 370.668±0.016	108 370.8(2) [21]
$\mu_{\rm d}$	0.333(5)	0.323–0.335 [20]
$W_{\rm d}$	0.28(3)	0.245–0.260 [20]
$q_{\rm d}$	1.38(10)	1.40–1.53 [20]

$$\epsilon_\ell = \frac{\tan[\pi(\nu_{J^+} + \mu_\ell)]}{W_\ell}. \tag{22}$$

In Eq. (21), $\sigma_{a\ell}$ and σ_b are the resonant and nonresonant contributions to the photoionization cross section, μ_ℓ, q_ℓ, and W_ℓ are the quantum defect, the quality factor, and the linewidth parameter for the $n\ell'$ resonances, and ν_{J^+} is the effective quantum number with respect to the $^2P_{J^+}$ threshold.

The photoionization spectra of ^{128}Xe, ^{130}Xe, ^{132}Xe, ^{134}Xe, and ^{136}Xe were analyzed by numerically fitting Eq. (21) to the experimental photoionization spectra in the range $\nu_{1/2}\approx 33$–42 and $\nu_{1/2}\approx 60$–92 to extract accurate ionization energies $^2P_{1/2}$ for the five xenon isotopes as well as line-shape parameters for the $nd'[3/2]_1$ resonances. The experimental spectra were recorded with a step size of 100 MHz and all points were used in the fitting procedure. Unambiguous line-shape parameters for the $ns'[1/2]_1$ resonances could not be obtained because the bandwidth of the laser and residual Doppler broadening (together about 0.01 cm^{-1}) contribute significantly to the spectral linewidth at the high n values of interest in the present study.

The value of the ionization energies were also derived independently by determining the central position of every s' and d' resonance in the range $\nu_{1/2}\approx 33$–42 and $\nu_{1/2}\approx 60$–110 and extrapolating the series to infinity using Rydberg's formula. The values obtained in both procedures agreed within the statistical uncertainties of the fits ($1\sigma = 0.002$ cm^{-1}). The ionization potential $^2P_{1/2}$ and the line-shape parameters of the d' resonances for ^{132}Xe are listed in Table I. Table II summarizes the isotopic shifts of the ionization energy for all other isotopes relative to that of ^{132}Xe as obtained in the procedure described above.

The value of (108 370.668±0.016) cm^{-1} for the $^2P_{1/2}$ ionization energy derived in this study is in agreement with the value of (108 370.8±0.2) cm^{-1} obtained by Yoshino [21] but not with the more recent value of (108 370.82±0.05) cm^{-1} determined by Kortyna *et al.* [22]. The accuracy of the isotope shifts of the ionization energy is limited by the statistical uncertainty ($1\sigma = 0.002$ cm^{-1}) of the fitting procedure. These isotope shifts agree, within the uncertainties of the respective determinations, with the values determined for the $^2P_{3/2}$ ionization energy by Brandi *et al.* [33]. The present results enable a determination of the spin-orbit splitting in Xe^+ to (10 536.879±0.019) cm^{-1}, which is isotope independent within the precision of our measurements. This value is compatible with the previous result of Yoshino and Freeman [21] but is an order of magnitude more precise.

B. Photoionization spectra of ^{129}Xe and ^{131}Xe

This subsection describes the experimental spectra of the xenon isotopes with $I\neq 0$ and their assignment. The assignments were made on the basis of MQDT simulations in an iterative procedure in which the MQDT parameters were refined and the assignments improved until a fully satisfactory agreement between MQDT predictions and experimental results was reached. The optimal MQDT simulations are already presented here together with the experimental results in the figures and, when necessary, also used to explain the experimental observations, although the fitting of the MQDT parameters is only discussed in the next subsection (Sec. IV C).

^{129}Xe has a nuclear spin $I=1/2$. A total of 6 s and 11 d channels with $F=1/2$ or $F=3/2$ are accessible following single-photon excitation from the $^1S_0$ ground state. Because of J mixing induced by the hyperfine interaction, the eigenchannels with $J=0$, 1, or 2 are required for the description of

TABLE II. Isotope shifts of the $^2P_{1/2}$ ionization energy relative to the position of the most abundant isotope ^{132}Xe. The ionization energies of the even mass number isotopes were derived in a least-squares fitting procedure of Eq. (21) to the photoionization spectra, and those for the odd mass number isotopes from the MQDT fit. These isotope shifts are compared to those determined at the $^2P_{3/2}$ threshold by Brandi *et al.* [33].

A	$[E_{\rm ion}(^2P_{1/2})(^A{\rm Xe}) - E_{\rm ion}(^2P_{1/2})(^{132}{\rm Xe})]/(hc\ {\rm cm}^{-1})$[a]	$[E_{\rm ion}(^2P_{3/2})(^A{\rm Xe}) - E_{\rm ion}(^2P_{3/2})(^{132}{\rm Xe})]/(hc\ {\rm cm}^{-1})$[b]
128	−0.0110(20)	−0.0134(30)
129	−0.0094(30)[c]	−0.0122(30)
130	−0.0057(20)	−0.0062(30)
131	−0.0030(30)[c]	−0.0067(30)
132	0	0
134	+0.0055(20)	+0.0060(30)
136	+0.0121(20)	+0.0150(30)

[a]This work.
[b]See Ref. [33].
[c]From MQDT analysis.

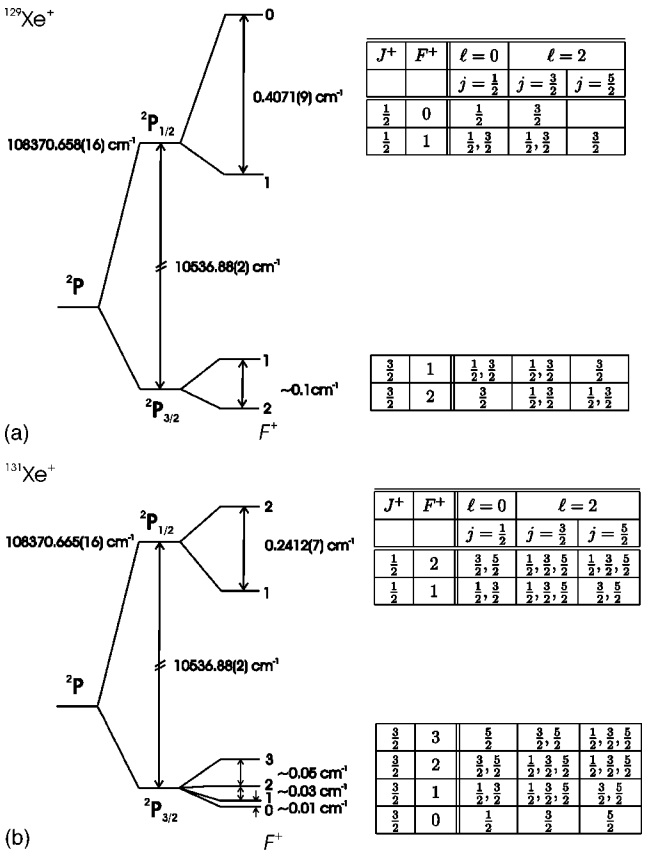

J^+	F^+	$\ell=0$	$\ell=2$	
		$j=\frac{1}{2}$	$j=\frac{3}{2}$	$j=\frac{5}{2}$
$\frac{1}{2}$	0	$\frac{1}{2}$	$\frac{3}{2}$	
$\frac{1}{2}$	1	$\frac{1}{2},\frac{3}{2}$	$\frac{1}{2},\frac{3}{2}$	$\frac{3}{2}$

$\frac{3}{2}$	1	$\frac{1}{2},\frac{3}{2}$	$\frac{1}{2},\frac{3}{2}$	$\frac{3}{2}$
$\frac{3}{2}$	2	$\frac{3}{2}$	$\frac{1}{2},\frac{3}{2}$	$\frac{1}{2},\frac{3}{2}$

J^+	F^+	$\ell=0$	$\ell=2$	
		$j=\frac{1}{2}$	$j=\frac{3}{2}$	$j=\frac{5}{2}$
$\frac{1}{2}$	2	$\frac{3}{2},\frac{5}{2}$	$\frac{1}{2},\frac{3}{2},\frac{5}{2}$	$\frac{1}{2},\frac{3}{2},\frac{5}{2}$
$\frac{1}{2}$	1	$\frac{1}{2},\frac{3}{2}$	$\frac{1}{2},\frac{3}{2},\frac{5}{2}$	$\frac{3}{2},\frac{5}{2}$

$\frac{3}{2}$	3	$\frac{5}{2}$	$\frac{3}{2},\frac{5}{2}$	$\frac{1}{2},\frac{3}{2},\frac{5}{2}$
$\frac{3}{2}$	2	$\frac{3}{2},\frac{5}{2}$	$\frac{1}{2},\frac{3}{2},\frac{5}{2}$	$\frac{1}{2},\frac{3}{2},\frac{5}{2}$
$\frac{3}{2}$	1	$\frac{1}{2},\frac{3}{2}$	$\frac{1}{2},\frac{3}{2},\frac{5}{2}$	$\frac{3}{2},\frac{5}{2}$
$\frac{3}{2}$	0	$\frac{1}{2}$	$\frac{3}{2}$	$\frac{5}{2}$

FIG. 2. Schematic energy-level diagram of the ^2P ground state of $^{129}Xe^+$ (a) and $^{131}Xe^+$ (b). The wave numbers given on the left of the diagram correspond to the $^2P_{1/2}\leftarrow{}^1S_0$ ionization energies and the wave numbers on the right represent the spin-orbit and hyperfine splittings determined in the present study. The tables list the total angular momentum quantum number F of all s and d dissociation channels associated with the $^2P_{J^+,F^+}$ ionic states.

the spectrum of ^{129}Xe. The fine and hyperfine structure of $^{129}Xe^+$ as it was determined from the analysis of the Rydberg spectrum (see below) is shown schematically on the left side of Fig. 2(a) which also lists all possible values of the J^+, F^+, ℓ, and j quantum numbers of the optically accessible dissociation channels. There are 3 s series and 4 d series converging to the $^2P_{1/2}$, $F^+=0$, 1 ionic states instead of 1 s and 1 d series in the case of the isotopes with zero nuclear spin.

The situation is more complex in ^{131}Xe ($I=3/2$), where a total of 10 s and 29 d channels with $F=1/2$, $3/2$, or $5/2$ are needed to describe the photoionization spectra obtained following single-photon excitation from the $^1S_0$ ground state. Close-coupling eigenchannels with $J=0$, 1, 2, 3, and 4 contribute to the spectrum, and 4 s and 11 d series converge to the $^2P_{1/2}$, $F^+=1$, 2 ionic states. The ionic level structure is shown schematically in Fig. 2(b) together with the quantum numbers of all dissociation channels.

The low-lying Rydberg states $5\leqslant\nu_{1/2}\leqslant 30$ are split by the hyperfine interactions but the observed resonances can still be classified in the extended jK-coupling scheme [Eq. (23)] in analogy to the situation encountered in the isotopes of zero nuclear spin,

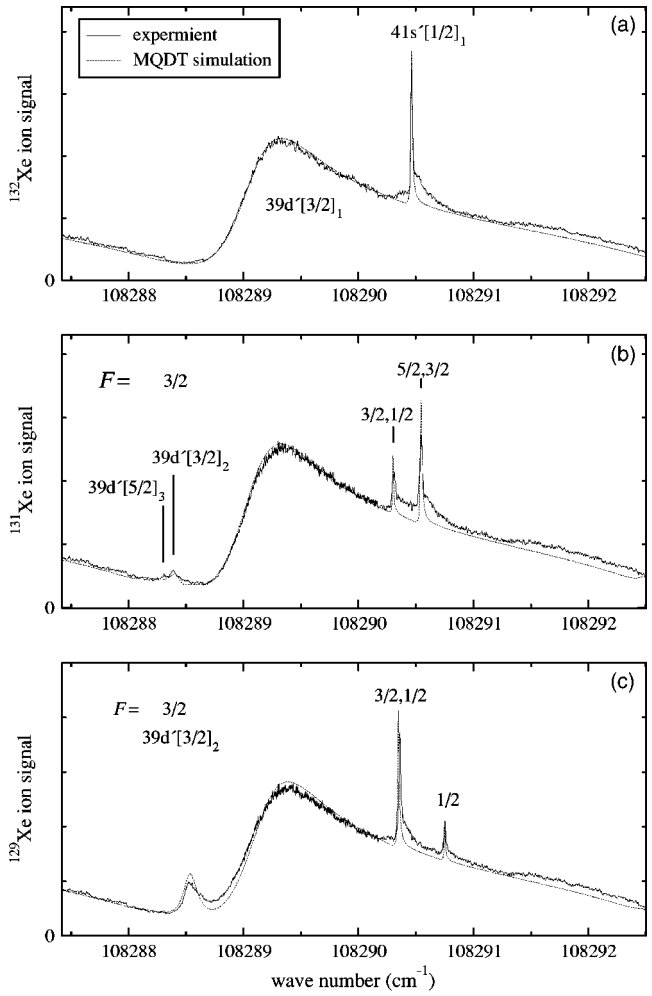

FIG. 3. Experimental relative photoionization cross section of xenon in the region of the $39d'[3/2]_1$ state (solid line) and its MQDT simulation (dotted line) for (a) ^{132}Xe, (b) ^{131}Xe, and (c) ^{129}Xe.

$$\vec{L}^+ + \vec{S}^+ = \vec{J}^+, \vec{J}^+ + \vec{\ell} = \vec{K}; \vec{K} + \vec{s} = \vec{J}, \vec{J} + \vec{I} = \vec{F}. \qquad (23)$$

Accordingly, the low-lying Rydberg states can be labeled in $n\ell'[K]_J(F)$ notation. In the high Rydberg states with $\nu_{1/2}\geqslant 65$, the Rydberg electron angular momentum $\vec{\ell}$ is decoupled from the core electronic angular momentum $\vec{J}^+$. In this range, the Rydberg series are characterized by a well defined ionic hyperfine state. The coupling scheme appropriate for this situation is given in Eq. (2) and is the one that was chosen for the dissociation channels.

The photoionization spectra of ^{132}Xe (a), ^{131}Xe (b), and ^{129}Xe (c) in the region of effective principal quantum number $\nu_{1/2}\approx 37$ are displayed in Fig. 3. The spectrum of ^{132}Xe (a) consists of the characteristic and well-known broad $39d'[3/2]_1$ and sharp $41s'[1/2]_1$ resonances. The spectra of the Fermionic isotopes reveal additional features that have their origin in hyperfine interactions. Two sharp resonances are observed in both spectra that can be assigned with the help of the MQDT simulation to distinct hyperfine components of s' resonances (see below). In the spectrum of ^{131}Xe, the lower sharp line consists of two overlapping s' reso-

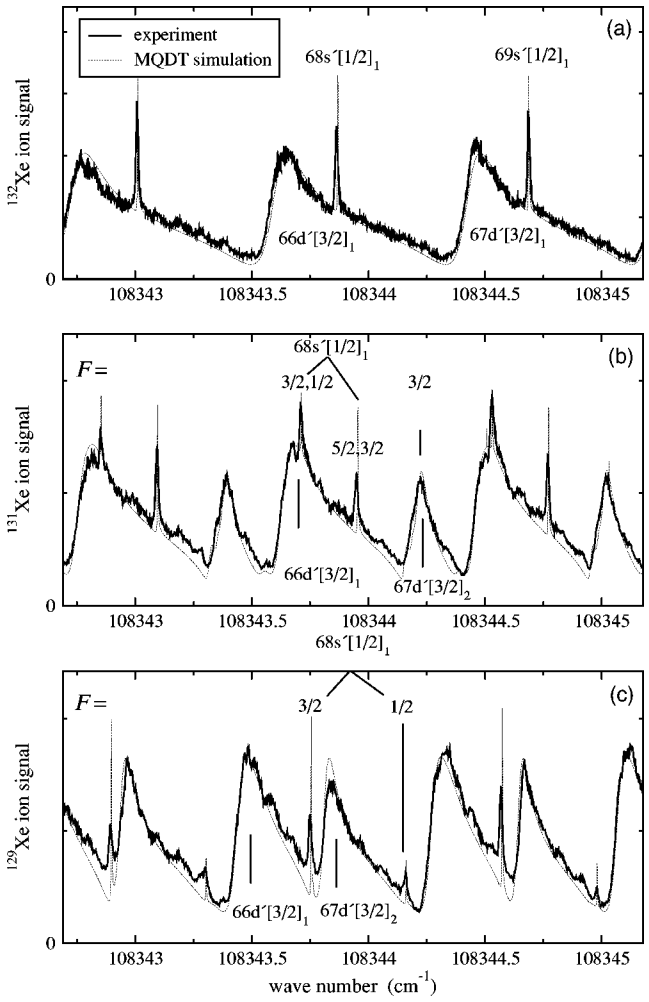

FIG. 4. Experimental relative photoionization cross section of xenon in the region of the $66d'[3/2]_1$ state (solid line) and its MQDT simulation (dotted line) for (a) ^{132}Xe, (b) ^{131}Xe, and (c) ^{129}Xe.

nances with $F=3/2$ and $1/2$, that belong to series converging on the $^2P_{1/2}$, $F^+=1$ ionic level, whereas the higher sharp line corresponds to s' resonances with $F=3/2$ and $5/2$ belonging to series converging on the $^2P_{1/2}$, $F^+=2$ ionic level. The situation is similar for ^{129}Xe where the lower line is a superposition of two s' resonances with $F=3/2$ and $1/2$ that belong to series converging on the $^2P_{1/2}$, $F^+=1$ level of $^{129}Xe^+$ and the higher line is a single s' resonance belonging to a series that converges on the $^2P_{1/2}$, $F^+=0$ ionic level.

The photoionization spectra of ^{131}Xe and ^{129}Xe also reveal a second d' resonance on the low wave-number side of the main d' line. This second line, assigned to the transition to the $39d'[3/2]_2$ level, originates from the relaxation of the selection rule on ΔJ resulting from the fact that the total angular momentum $\vec{F}$ is the conserved quantity in the presence of nuclear spin.

At higher values of the principal quantum number, the spectra of ^{129}Xe and ^{131}Xe begin to differ markedly from the spectrum of ^{132}Xe and from each other as illustrated in Fig. 4 where the spectra of ^{132}Xe (a), ^{131}Xe (b), and ^{129}Xe (c) around $\nu_{1/2}\approx 65$ are compared. The reason for this behavior is that J mixing is almost complete around $\nu_{1/2}\approx 65$, so that the $nd'[3/2]_2$ resonances become as intense as the $nd'[3/2]_1$ resonances. In Fig. 4, the resonances are labeled by the ℓ and F values of the most significant contribution according to the MQDT simulations.

The nuclear spins have the following effects on the photoionization spectra of ^{129}Xe and ^{131}Xe as compared to the isotopes with zero nuclear spin: First, $\vec{F}$ and not $\vec{J}$ is the constant of motion in the presence of nuclear spin, and therefore additional nd' resonances are observed above $\nu_{1/2}\approx 30$ that can be assigned to $J=2$ with a weak $J=3$ contribution [see, e.g., Fig. 3(b)]. Around $\nu_{1/2}\approx 65$, J mixing is complete and nearly equally intense d' resonances are observed for both $J=1$ and $J=2$ (Fig. 4). The integrated intensity of the $nd'[3/2]_2$ resonances, however, is weaker in the case of ^{131}Xe than it is in ^{129}Xe, reflecting the weaker hyperfine interaction in the ion (see Table IV below). Second, the uncoupling of the Rydberg electron from the core leads to the observation of series that converge on different hyperfine states of the ion. Strong perturbations of line positions and intensities arise when Rydberg states converging on different ionic states become nearly degenerate. The hyperfine interaction between quasibound states of the same total angular momentum F but different principal quantum numbers then induces a strong mixing of these states that causes intensity alterations in the spectrum.

These effects are illustrated by the MQDT calculations presented in Fig. 5, which displays the predicted photoionization cross section associated with the $F=3/2$ channels of ^{129}Xe [Fig. 5(a)] and the fractional part of the effective quantum number $\nu_{J^+=1/2,F^+=1}$ [Fig. 5(b)] of the s' and the three d' quasibound levels plotted against $\nu_{1/2,1}$. The s' series and two of the d' series have a constant quantum defect and therefore correspond to channels that are built on a $^2P_{1/2}$, $F^+=1$ core. The remaining d' series converges to the higher $^2P_{1/2}$, $F^+=0$ state of the ion and therefore regularly traverses the other series, leading to a series of avoided crossings. In order to understand the intensity distribution in the spectrum, the series must be correlated with close-coupling channels at low values of the effective quantum number $5\leqslant\nu_{J^+=1/2,F^+=1}\leqslant 30$. Figure 5 reveals that the d' series converging to the higher $^2P_{1/2}$, $F^+=0$ state of the ion carries the intensity in the low-energy part of the spectrum. Indeed this series correlates at low n with the p^5d, $^1P_1$ channel, which is the only d channel carrying intensity [see the left-hand side of Fig. 5(b)]. A very similar situation is also encountered for the ^{131}Xe isotope (see discussion of Fig. 6 below).

As a consequence of the angular momentum uncoupling that takes place at higher n values, the intensity spreads from the $J=1$ d' series into the lower of the two d' series associated with a $J=2$ close-coupling channel [see Fig. 5(b)]. As observed experimentally (see Fig. 6), the intensity of the d' series converging on the $^2P_{1/2}$, $F^+=1$ level vanishes at the position of the avoided crossings because the hyperfine interaction between the series leads to a very small $p^5d\ ^1P_1$ character.

In the photoionization spectrum of ^{129}Xe [see Fig. 6(a)], two strong d' series ($nd'[3/2]_1$ and $nd'[3/2]_2$) are observed, the former converging to the $F^+=0$, the latter to the $F^+=1$

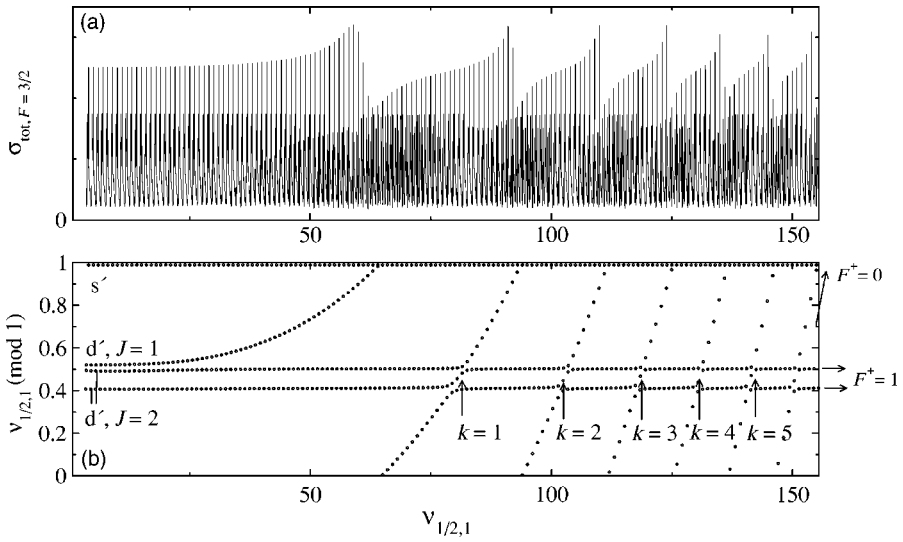

FIG. 5. MQDT simulation of the contribution to the photoionization cross section of ^{129}Xe from s' and d' series with $F=3/2$ (a) and effective quantum numbers $\nu_{J^+=1/2,F^+=1}$(mod 1) of the quasibound states corresponding to the four $F=3/2$ series (b). The dots lying on a line on top of (b) correspond to the s' series, while the others belong to the d' series. The abscissa is the effective quantum number $\nu_{1/2,1}$.

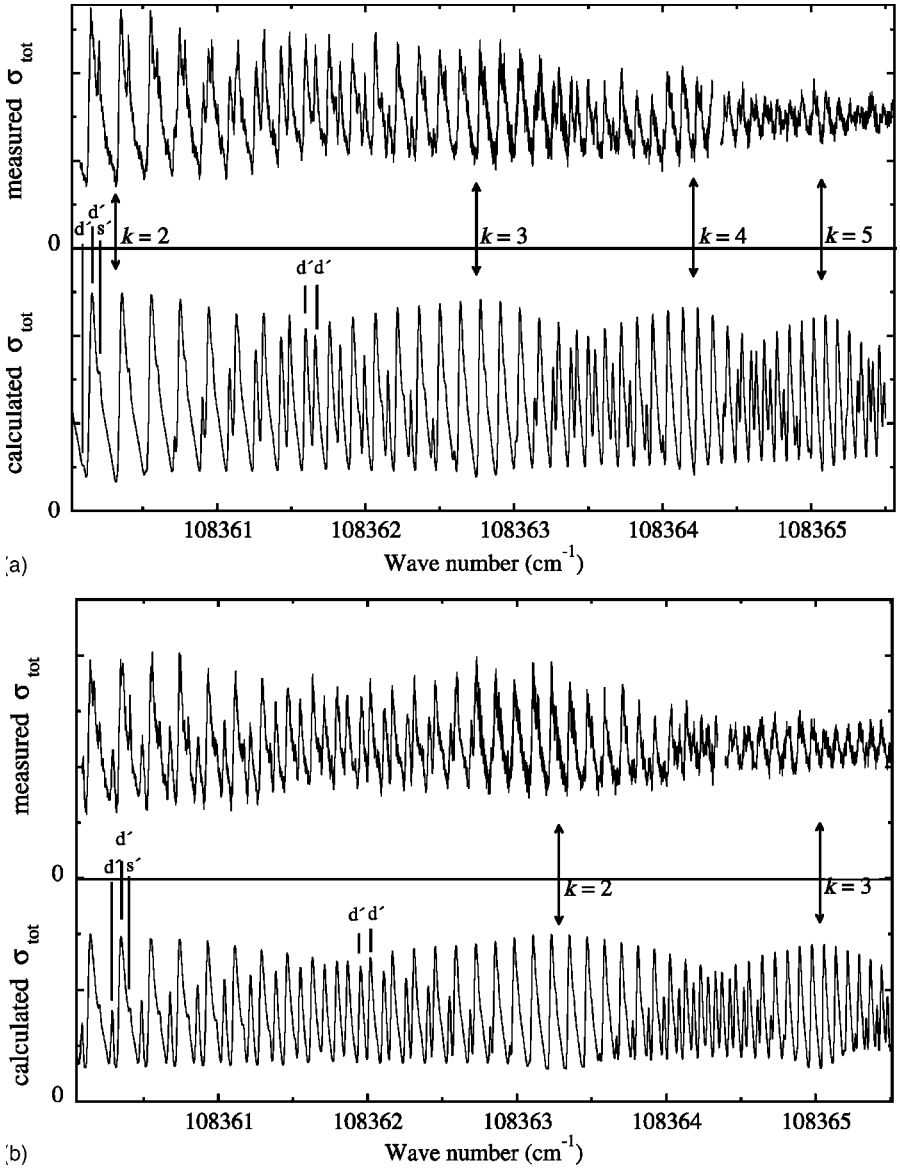

FIG. 6. Experimental relative photoionization cross section (upper trace) and its MQDT simulation (lower trace) of ^{129}Xe (a) and ^{131}Xe (b), in the region of effective quantum number $\nu_{1/2}=100$–150. The photoionization profiles calculated by MQDT have been convoluted with a Gaussian of full width at half maximum 0.011 cm^{-1} in order to account for the finite bandwidth of the vuv laser.

ionic hyperfine levels. The intensity of the second series vanishes at the positions where its members become degenerate with members of the first series. This is the case when the hyperfine splitting of two ionic levels $\Delta E_{F^+,F^+ +1}$ becomes equal to the spacing between the Rydberg states n and $n+k$ [43], a condition that can be expressed as

$$\Delta E_{F^+,F^+ +1} \approx k\frac{2R_M}{n^3}, \tag{24}$$

with $F^+=0$ for the $^2P_{1/2}$ ionization limit of ^{129}Xe. Successive positions of near degeneracy and the corresponding k values are indicated by vertical arrows in Fig. 6. In the spectra of ^{129}Xe [Fig. 6(a)], these n-mixing perturbations induced by the hyperfine interactions are observed up to $k=5$. They are more sparse in the spectrum of ^{131}Xe because of the smaller splitting between the $F^+=1$ and 2 hyperfine levels of $^{131}Xe^+$ and occur only for $k=2$ and 3 in the spectrum of Fig. 6(b). Comparable intensity alterations have also been observed in the spectrum of the high bound Rydberg states of ^{83}Kr($n \geqslant 100$) [11]. The effects discussed above can be understood in a simple physical picture: At the position where the effective quantum numbers are related by $\nu_{F^+ +1}=\nu_{F^+}+k$ with k integer, the Rydberg electron orbital period is equal to k times the precession period of $\vec{F}^+$ around $\vec{J}^+$ which implies that the Rydberg electron "sees" a core with vanishing hyperfine structure. The analogous situation for a rotating molecular core was described by Labastie *et al.* [44]

C. Numerical fitting of the MQDT parameters

The adjustable parameters needed for the MQDT simulation of the photoionization spectra are the eigenquantum defects μ_α, which are assumed to be unaffected by the hyperfine interaction, the value of the (center of gravity) ionization energies corresponding to the formation of the $^2P_{3/2}$ and $^2P_{1/2}$ ionic states, the magnetic dipole hyperfine coupling constants of $^{129}Xe^+$ and $^{131}Xe^+$, and the electric quadrupole hyperfine coupling constant of $^{131}Xe^+$. The magnetic octupole hyperfine coupling of $^{131}Xe^+$ is negligible in the present context.

In the analysis of the spectra the quantum defects μ_α available from the literature were adjusted iteratively. First, an MQDT simulation of the ^{132}Xe photoionization spectrum was undertaken using the different sets of quantum defects and corresponding $U_{i\alpha}$ matrices published in Refs. [6,19,23], but none of them reproduced the experimental line shapes in a fully satisfactory manner, probably because of the energy dependence of the eigenquantum defects. The only available channel parameters ($J=1$) taking the departure of close-coupling channels from *LS* coupling into account did not reproduce the spectrum as well as achieved by a simple adjustment of the eigenquantum defects in *LS* representation. Realizing that too little information is contained in the photoionization spectra alone for a determination of the exact eigenchannels and eigenquantum defects, we therefore decided to neglect the departure of the close-coupling channels from *LS* coupling.

In a first step, the five quantum defects $\mu_\alpha(J=1)$ were adjusted manually until a good agreement with the experimental spectra of ^{132}Xe was reached. In this adjustment the ionization energy derived in Sec. IV A was used (see Table I).

With these adjusted eigenquantum defects for the $J=1$ channels and initial values for the $J=0$ and $J=2$ eigenquantum defects estimated from the quantum defect analysis of Ref. [29], an MQDT simulation of the ns' photoionization resonances of ^{129}Xe was performed. The s' resonances in the experimental spectra could be assigned on the basis of their relative intensities and the comparison with the MQDT predictions. ^{129}Xe possesses two s' series converging to the $^2P_{1/2}$, $F^+=1$ ionization limit with $F=1/2$ and $F=3/2$ and one s' series with $F=1/2$ converging to the $^2P_{1/2}$, $F^+=0$ level [see Fig. 2(a)]. The $F=3/2$ resonances are calculated to be stronger than those with $F=1/2$. By inspection of Fig. 3 one can thus conclude that the $F=3/2$ levels in ^{129}Xe lie below the $F=1/2$ levels. In ^{131}Xe, two s' series converge to each of the $^2P_{1/2}$, $F^+=1$ and $^2P_{1/2}$, $F^+=2$ states with total angular momentum quantum numbers $F=1/2$, $3/2$ and $F=3/2$, $5/2$, respectively. The observed intensities indicate that the levels with $F=1/2$, $3/2$ lie below those with $F=3/2$, $5/2$. These observations imply that the magnetic dipole coupling constants of the two isotopes have an opposite sign.

In a nonlinear least-squares fitting procedure of the calculated positions of the $F=3/2$ and $F=1/2$ s' resonances to the experimental positions determined in a least-squares fit using Eq. (21), a preliminary value of the magnetic dipole hyperfine coupling constant $^{129}A_{1/2}$ was derived. In the next step, the eigenquantum defects of the s channels with $J=0$ and $J=2$ and of the d channels with $J=2$ were adjusted manually in order to reproduce the line shapes and line positions in the spectrum of ^{129}Xe. Finally, the least-squares fitting procedure of $^{129}A_{1/2}$ and the ionization energy was repeated with the improved quantum defects, and a final value of $^{129}A_{1/2}$ [$^{129}A_{1/2}=-0.4071(9)\text{cm}^{-1}$] was derived. At this stage, a satisfactory agreement between the experimental spectra and the MQDT simulation was reached, as can be seen from a comparison of calculated and experimental traces in Figs. 3, 4, and 6.

A similar procedure was followed to simulate the spectra of ^{131}Xe where additional eigenquantum defects for the $J=0$, 3, 4 d channels were required. It turned out, however, that the $J=0$ and $J=4$ eigenquantum defects do not affect the line shapes and line positions. In fact, no quasibound d Rydberg states with $J=0$ or $J=4$ are found between the $^2P_{3/2}$ and $^2P_{1/2}$ ionic limits, so that the $J=0$ and $J=4$ channels consist almost exclusively of contributions from open channels in this region.

The eigenquantum defects obtained in the MQDT analysis and the values of the magnetic dipole hyperfine constants $A_{1/2}$ are listed in Tables III and IV, respectively. The ratio $^{129}A_{1/2}/^{131}A_{1/2}$ provides a consistency check of the hyperfine constants. The magnetic dipole constant $A_{1/2}$ is proportional to the ratio of the nuclear magnetic moment μ and the nuclear spin quantum number I, thus $^{129}A_{1/2}/^{131}A_{1/2}=(\mu^{129}I^{131})/(\mu^{131}I^{129})$. The ratio of the constants determined in this work $^{129}A_{1/2}/^{131}A_{1/2}=-3.375(12)$ corresponds well to the value $^{129}A_{1/2}/^{131}A_{1/2}=-3.373\,41$ obtained using the literature values $\mu^{129}=-0.777\,977\,\mu_N$ and $\mu^{131}=0.691\,861\,\mu_N$ from Ref. [45].

TABLE III. Term symbols of all *LS* coupled eigenchannels included in the present MQDT model and eigenquantum defects determined by fitting the MQDT model parameters to the experimental spectra as explained in the text.

Close-coupling channels	μ_α [a]
$s\,^3P_0$	0.015
$s\,^1P_1$	−0.022
$s\,^3P_1$	0.0285
$s\,^3P_2$	0.030
$d\,^3P_0$	0.545[b]
$d\,^1P_1$	0.140
$d\,^3P_1$	0.615
$d\,^3D_1$	0.375
$d\,^3P_2$	0.615
$d\,^1D_2$	0.544
$d\,^3D_2$	0.340
$d\,^3F_2$	0.475
$d\,^3D_3$	0.360
$d\,^1F_3$	0.455
$d\,^3F_3$	0.475
$d\,^3F_4$	0.475[b]

[a]Determined in this work.
[b]Unmodified from Ref. [29].

An accurate determination of the hyperfine structure of the $^2P_{3/2}$ state of $^{129}Xe^+$ and $^{131}Xe^+$ following the procedure of Ref. [11] requires the analysis of the hyperfine structure in the bound Rydberg series of these isotopes. Unfortunately, the hyperfine structure has only been resolved for a few low-lying states with principal quantum numbers $n=5$–8. The description of the absolute position of these states requires one to take into account at least the energy dependence of the eigenquantum defects. To estimate the hyperfine structure of the $^2P_{3/2}$ state, we have chosen the highest Rydberg states for which the hyperfine structure has been resolved, i.e., $8d[3/2]_1$ and $8d[1/2]_1$ [33]. A fit of the MQDT model to the hyperfine structure of these states in ^{129}Xe and ^{131}Xe provides a rough estimate of the electric dipole and magnetic quadrupole hyperfine coupling constants $A_{3/2}$ and $B_{3/2}$. No fully satisfactory fit could be reached, however, probably because of the unsatisfactory description of the energy dependence of the quantum defects and the deviation from *LS* coupling. The relative deviations between measured and calculated hyperfine intervals vary between 6% and 40%. The hyperfine constants are therefore characterized by large uncertainties (see Table IV).

TABLE IV. Magnetic dipole (A_{J^+}) and electric quadrupole (B_{J^+}) hyperfine coupling constants for the $^2P_{J^+}$ states of $^{129}Xe^+$ and $^{131}Xe^+$. The constants for the $^2P_{1/2}$ states were derived from the MQDT analysis of the present experimental results, whereas the $^2P_{3/2}$ constants were derived from an MQDT fit using the hyperfine structure of low-lying bound Rydberg states as detailed in the text.

Isotope	$A_{1/2}$ (cm^{-1})	$A_{3/2}$ (cm^{-1})	$B_{3/2}$ (cm^{-1})
^{129}Xe	−0.4071(9)	≈−0.054(15)	
^{131}Xe	0.1206(3)	≈0.014(5)	≈0.006(5)

The comparison of experimental and simulated spectra in Figs. 3, 4, and 6 demonstrates that the present MQDT model provides an adequate description of the line positions, line intensities and line shapes of both $I=0$ and $I\neq 0$ isotopes in the autoionization regions of Xe. The main deviations between calculated and experimental spectra occur in the s' resonances which appear more intense and narrower in the simulations than in the experimental spectra. These deviations can be fully explained by the limited resolution of the present experiments as already mentioned above. A weak shoulder on the high-energy side of the s' resonances in the spectra of all isotopes (see Fig. 3) is also not accounted for satisfactorily by the simulations. At present we have no explanation for this structure, and cannot rule out that it is caused by a (Doppler-broadened) contribution from the background gas.

V. DISCUSSION

A. Limitations of the present MQDT model

Multichannel quantum defect theory describes the structure of Rydberg states with an accuracy comparable to the highest resolution of current spectroscopic methods [12]. This theory relies on the description of the interactions in the limiting coupling cases where the Rydberg electron is very close to the ionic core (close-coupling region) and very far from the core (dissociation region). The inclusion of the nuclear spin into the MQDT formalism for the rare-gas atoms provides an opportunity to reconsider the description of both coupling cases and to discuss the major approximations.

In the close-coupling region, the electrostatic interactions (orbit-orbit and exchange) dominate the level structure. An adequate description is therefore provided by *LS* coupling. The orbit-orbit and exchange interactions translate into differences in the values of the eigenquantum defects. This description neglects all other interactions in the core. As was pointed out by Lu [6], the spin-orbit and *s*-*d* interactions lead to a mixing of the pure *LS*-coupled channels and can be accounted for by modifying the transformation matrix and the quantum defects. For nuclei with $I\neq 0$, an additional mixing of the close-coupling channels can in principle be induced by the hyperfine interactions. However, these interactions are so much weaker, in the rare-gas atoms, than the spin-orbit and exchange interactions, that they can be neglected in excellent approximation in the description of the short-range eigenchannels [11].

In the dissociation region, the dominant interactions are those in the ionic core, i.e., the spin-orbit and hyperfine interactions. Since the magnitude of these interactions differs by roughly four orders of magnitude in the ^2P ground state of the singly charged rare-gas cations, the coupling case chosen in Eq. (2) is easily justifiable. Neglecting the hyperfine in-

duced mixing of the ionic spin-orbit levels is thus expected to be an excellent approximation.

An exact description of N_s close-coupling s and N_d d channels of the same total angular momentum requires the determination of $(N_s+N_d)(N_s+N_d-1)/2$ independent matrix elements or generalized Euler angles [6] and their energy dependence. If the s-d interaction is neglected, this number reduces to $N_s(N_s-1)/2+N_d(N_d-1)/2$. Given that the hyperfine induced mixing of the eigenchannels can be neglected (see above), this number is further reduced because only close-coupling channels with the same quantum number J are allowed to interact. It is, however, known [6] that the numerical fitting of the MQDT parameters to photoionization spectra does not provide sufficient information to derive a complete description of the eigenchannels. Indeed, when several series converge onto a common ionization threshold, the spectra of Rydberg states alone are insufficient for the derivation of unambiguous channel parameters, and additional information (not currently available) on the wave functions of the considered states is required.

To alleviate some of these difficulties we chose, in the present analysis, to approximate the close-coupling channels by pure LS coupled channels, and to adjust the corresponding quantum defects. This approximation implies that autoionization, as described by the present model, is only determined by the electrostatic close-coupling interactions. More specifically, the exchange interaction between the $^3P_1$ and $^1P_1$ configurations leads to the autoionization of the s' states and the additional orbit-orbit interaction in the $^3D_1$ configuration induces the autoionization of the d' states. The advantage of this procedure is that it enables us to highlight the salient features of the hyperfine autoionization and to demonstrate that it is not caused by the hyperfine interaction. Moreover, despite the approximation, the model can quantitatively account for the spectra because the eigenquantum defects can be adjusted as effective constants to reproduce the experimental spectra, and also to adequately describe the positions and dynamics of the autoionizing Rydberg states. The drawback is that the constants determined in this work are only valid over a restricted energy range and do not provide a quantitatively correct representation of the complete xenon spectrum below, between and above the two ^2P ionization thresholds. A complete and fully satisfactory set of MQDT parameters for the xenon atom remains to be derived.

B. Hyperfine and spin-orbit autoionization

The results presented so far show that the phenomenon of spin-orbit autoionization in the presence of a nonzero nuclear spin can be well understood and interpreted with the help of an MQDT model. The same framework also provides a description of hyperfine autoionization and a characterization of the underlying mechanisms. In what follows we show some predictions of autoionizing spectra involving hyperfine autoionization. The observation of this phenomenon has been impossible so far, because the small magnitude of the hyperfine splittings of the ion ($0.41\ \mathrm{cm}^{-1}$ in the $^2P_{1/2}$ state of $^{129}Xe^+$, and typically much less in lighter atoms and molecules) sets a lower limit of $n \approx 520$ for the principal quantum number of the autoionizing Rydberg states to be observed, which represents an experimental challenge.

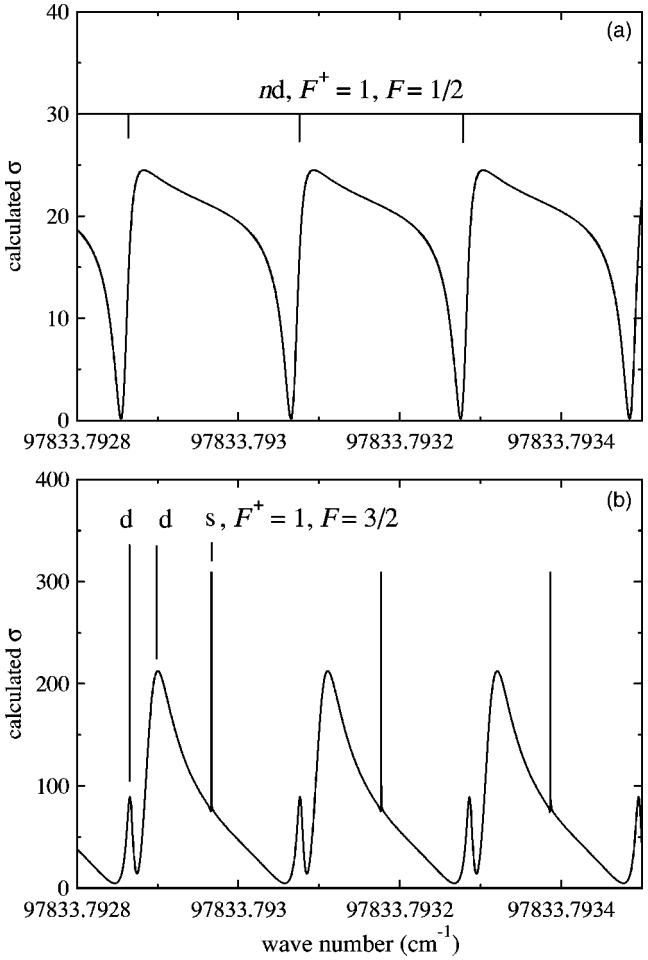

FIG. 7. MQDT prediction of the relative photoionization cross section of ^{129}Xe in the region between the $^2P_{3/2}$, $F^+=2$ and 1 ionic hyperfine states. The displayed structures result from pure hyperfine autoionization. The contributions from the $F=1/2$, $3/2$ manifolds are shown in panels (a) and (b), respectively.

The MQDT model used here represents an adequate framework to discuss the mechanism and the propensity rules that govern autoionization. In the discussion, it is convenient to distinguish between three energetic regions. The first region is that between the lowest and the highest hyperfine component of the $^2P_{3/2}$ state. The second region is located between the highest hyperfine component of the $^2P_{3/2}$ state and the lowest component of the $^2P_{1/2}$ state, and the third corresponds to the region between the lowest and the highest hyperfine component of the $^2P_{1/2}$ state.

At first sight, spin-orbit and hyperfine autoionization would be expected to follow entirely different dynamics because the energy transfered between the ion core and the Rydberg electron in the two processes differs by several orders of magnitude. However, as discussed above, both processes have their origin in electrostatic (orbit-orbit and exchange) interactions, and are therefore governed by the same dynamics, determined by the values of the eigenquantum defects. The branching ratios for autoionization into various dissociation channels depend only on the values of the quan-

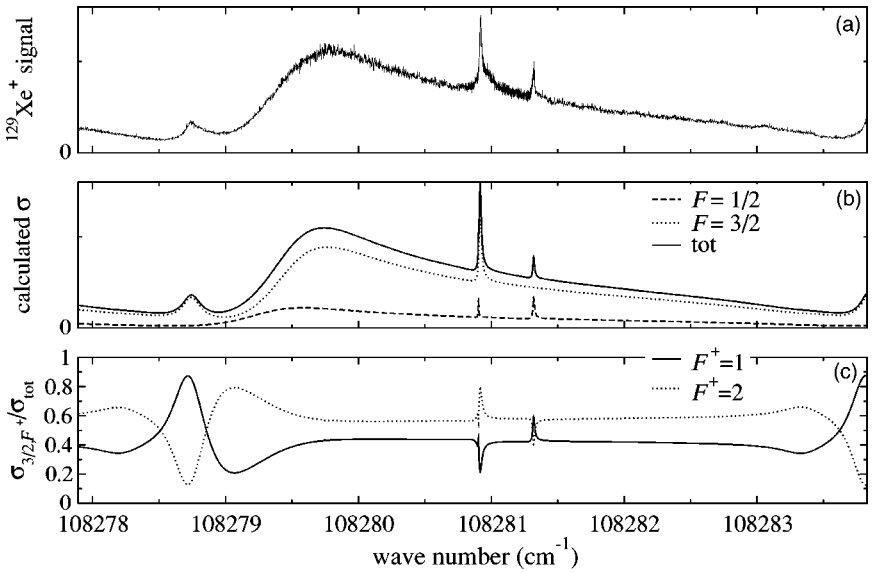

FIG. 8. (a) Experimental relative photoionization cross section of ^{129}Xe in the region of the $37d'[3/2]_1$ state, (b) MQDT simulation of the total cross section (solid line), the contribution from $F=1/2$ states (dotted line), and $F=3/2$ states (dashed line), (c) branching ratios into the ionization channels leading to an ion in the $^2P_{3/2}$, $F^+=1$ (solid line) and $^2P_{3/2}$, $F^+=2$ (dotted line).

tum numbers, or more specifically on the values of the transformation matrix $U_{i\alpha}$.

1. Hyperfine autoionization within the $^2P_{3/2}$ sublevels

A simple situation of pure hyperfine autoionization occurs in the region between the $^2P_{3/2}$, $F^+=2$ and $F^+=1$ states of $^{129}Xe^+$ [see Fig. 2(a)] for which two sets of channels, with $F=1/2$ and $F=3/2$, can be treated separately. In the $F=1/2$ manifold, a single quasibound d' series converging to the $F^+=1$ level exists, which interacts with two degenerate $F^+=2$ continua. To characterize the autoionization dynamics in this region, the photoionization cross section predicted by MQDT and shown in Fig. 7(a) was analyzed with the parametrization of Eq. (21) resulting in parameters $W=0.151$ or $\Gamma_r=2.11\times10^4$ cm^{-1} and $q=0.403$. Figure 7(b) represents the contribution to the photoionization cross section from the $F=3/2$ manifold. In this case, one s and two d quasibound series interact with one s and two d continua. Since the s series does not interact with the d series, it can be analyzed separately with the two-channel formula [Eq. (21)]. A numerical fit of the isolated s series led to the parameters $W=8.25\times10^{-4}$ (or $\Gamma_r=115$ cm^{-1}) and $q=128$.

The reduced widths $\Gamma_{r\ell}$ are independent of n and directly reflect the strength of the channel interactions. They can thus be used to compare the dynamics of pure hyperfine autoionization with that of spin-orbit autoionization of the s' and d' series of ^{132}Xe. Analyzing the MQDT prediction of the photoionization cross section with Eq. (21) yields the following parameters for the s' and d' series of ^{132}Xe: $W_d=0.277$ (or $\Gamma_{r,d}=3.87\times10^4$cm^{-1}) and $q_d=1.49$ and $W_s=5.61\times10^{-3}$ (or $\Gamma_{r,s}=783$ cm^{-1}) and $q_s=9.40$. The values obtained for the d' series slightly differ from those listed in Table I because they resulted from a fit to the MQDT calculation whereas the latter were determined in a fit to the experimental spectrum. The discrepancy lies within the statistical uncertainty. Although one might have naively expected much slower dynamics for the hyperfine autoionization than for spin-orbit autoionization, the comparison of the reduced widths of the s and d resonances leads to the conclusion that the channel interactions causing spin-orbit and hyperfine autoionization have a comparable strength. Hyperfine autoionization is thus an allowed and even a very efficient process in the rare-gas atoms.

2. ΔF^+ propensity rules in spin-orbit autoionization

In the region above the $^2P_{3/2}$ ionization limit, the Rydberg states converging to the $^2P_{1/2}$ state decay by spin-orbit autoionization to a $^2P_{3/2}$ Xe^+ ion and a free electron. In the case of ^{129}Xe and ^{131}Xe, the ions can be produced in different hyperfine states. The question naturally arises whether the autoionization could be used as a means to produce ions in selected hyperfine levels. The experimental discrimination between different hyperfine product channels, for instance by high-resolution photoelectron spectroscopy, is currently not possible, but the MQDT model developed in the present work allows quantitative predictions of the partial photoionization cross sections to selected ionic hyperfine structure levels to be made [see Eq. (14)].

The calculated partial cross sections show resonances similar to those of the total cross section (see Sec. III). As a consequence of multiple interferences, spectral regions can be identified in which partial cross sections to a selected ionic hyperfine state dominate. Unfortunately, when many different ionic states are energetically accessible, the minima of the partial cross sections do not usually coincide, and therefore the entirely selective production of a single ionic hyperfine level is rarely possible. The maximal contrast between different hyperfine channels is therefore expected when only two ionic hyperfine states are available as in the case of the $^2P_{3/2}$ ground state of $^{129}Xe^+$.

Such a case is illustrated in Fig. 8 where the experimental total cross section [Fig. 8(a)], the calculated cross section with the contributions from $F=3/2$ and $F=1/2$ [Fig. 8(b)] and the branching ratios between the two ionic hyperfine states of $^{129}Xe^+$ [Fig. 8(c)] are represented. An inspection of the partial cross sections enables one to identify regions where the branching ratio between the $^2P_{3/2}$, $F^+=2$, and $F^+=1$ states of $^{129}Xe^+$ is extremal. For instance, more than

85% of the ions are produced in the $F^+=1$ state at a photon wave number of $(108\,278.72\pm0.02)\,\mathrm{cm}^{-1}$, whereas at $(108\,279.1\pm0.1)\,\mathrm{cm}^{-1}$ close to 80% of the ions are produced in the $F^+=2$ state.

These results show that it is possible to produce hyperfine selected ions through photoionization by exploiting the interference of the atomic channels. Indeed, the widths of the resonances in the partial cross sections are large enough that a selective production of hyperfine levels should be possible using broadly available lasers. This conclusion is expected to be valid for many other ions that possess a hyperfine doublet in the ground state. This is in particular the case for the odd mass number isotopes of earth-alkaline metals which are of interest in ion trap loading [17] and its applications to quantum computation [18].

3. Competition between hyperfine and spin-orbit autoionization in the $^2P_{1/2}$ levels

In the region between the two hyperfine components of the $^2P_{1/2}$ state of $^{129}Xe^+$ and $^{131}Xe^+$ the competition between pure hyperfine and spin-orbit autoionization can be studied. In what follows, a few cases with specified values of ℓ and F are discussed and some general propensity rules are derived.

We first consider the s' series of ^{129}Xe with $F=1/2$ converging on the $F^+=0$ hyperfine level [see Fig. 2(a)]. The associated Rydberg states can autoionize in either the $^2P_{1/2}$ $F^+=1$ ϵs open channel (hyperfine autoionization) or the $^2P_{3/2}$ $F^+=1$ ϵs open channel (spin-orbit autoionization). The partial cross sections corresponding to these two processes calculated by MQDT can again be analyzed with the parametrization of Eq. (21). The width parameter obtained in both cases is exactly the same ($W=4.30\times10^{-3}$) because it is a property of the quasibound state. The resonant cross section σ_a is 8.0 times larger for spin-orbit autoionization. The considered s' states therefore preferentially decay via spin-orbit autoionization.

A similar situation is found in the $F=3/2$ s' series of ^{131}Xe converging on the $F^+=2$ ionic level [see Fig. 2(b)]. The members of this series can decay into the $^2P_{1/2}$, $F^+=1$, the $^2P_{3/2}$, $F^+=2$ or the $^2P_{3/2}$, $F^+=1$ continua. The partial cross sections for these processes are characterized by the resonant cross sections $\sigma_a=0.209$, 0.502, and 0.167, respectively, and the width parameter amounts to $W=2.12\times10^{-3}$. In this case, hyperfine autoionization efficiently competes with spin-orbit autoionization with a resonant cross section intermediate between that of the two spin-orbit contributions. In addition, it is noted that $\Delta F^+=0$ is preferred over $\Delta F^+=-1$ for spin-orbit autoionization.

The situation for the d' series in ^{131}Xe is even more interesting because more open channels are available [see Fig. 2(b)]. Two cases are presented which are extremal concerning the values of resonant cross sections. The $F=1/2$ manifold holds two almost degenerate quasibound d' series converging to the $^2P_{1/2}$, $F^+=2$ level. These d' levels can autoionize in any one of the five continua with $^2P_{1/2}$, $F^+=1$ and $^2P_{3/2}$, $F^+=3$, 2, 2, 1. The situation of two closed channels having a common ionization threshold and five open channels can be approximated by the parametrization for one open and two closed channels [42],

$$\sigma=\sigma_a\frac{\left(1+\sum_{j\in Q}\frac{q_j}{\epsilon_j}\right)^2}{1+\left(\sum_{j\in Q}\frac{1}{\epsilon_j}\right)^2}+\sigma_b, \tag{25}$$

where the symbols have the same meaning as in Eq. (21). In Eq. (25), a nonresonant cross section σ_b has been added to Eq. 25 of Ref. [42]. Although this parametrization is not exact, it turned out to provide an excellent fit of the calculated partial cross sections. The ratio of the resonant cross sections are found to be $\sigma(1/2,1):\sigma(3/2,3):\sigma(3/2,2):\sigma(3/2,1)=0.155:3.40:0.555:0.104$. Considering the number of open channels built on each ionic state which is 1:1:2:1, the resonant partial cross sections are highly nonstatistical and the autoionization dynamics is characterized by a strong preference for $\Delta F^+=+1$ over $\Delta F^+=0$ over $\Delta F^+=-1$ in spin-orbit autoionization. Again, hyperfine autoionization has a significant contribution.

The $F=5/2$ manifold also holds two quasibound d' series converging to the $^2P_{1/2}$, $F^+=2$ level. These d' levels can autoionize in any one of the two $^2P_{1/2}$, $F^+=1$ and $^2P_{3/2}$, $F^+=3$, 3, 2, 2, 1, 1, 0 continua. The same analysis as presented above for the $F=1/2$ case leads to the ratio of resonant cross sections $\sigma(1/2,1):\sigma(3/2,3):\sigma(3/2,2):\sigma(3/2,1):\sigma(3/2,0)=11.5:10.6:9.6:9.2:4.7$. This ratio corresponds closely to a statistical expectation since the ratio of the number of open channels is 2:2:2:2:1. Nevertheless, a slight preference for $\Delta F^+=+1$ over $\Delta F^+=0$ over $\Delta F^+=-1$ is found again, and hyperfine autoionization even represents the most important contribution to the total cross section.

Two conclusions are drawn from the above results. First, the rate of autoionization for hyperfine and spin-orbit autoionization is comparable as already pointed out in Sec. V B 1 above. Second, the propensity rule for the spin-orbit autoionization favors processes in which $\Delta F^+=\Delta J^+$, and is most pronounced for small values ($F=1/2$) of the total angular momentum, whereas at larger values ($F=5/2$) the partitioning is close to statistical. These observations can be interpreted by analyzing the properties of the angular momentum recoupling matrix elements (the values of the $3j$ symbols become equal in the limit of high quantum number) and represent a geometric effect.

VI. CONCLUSIONS

The photoionization spectra of ^{129}Xe and ^{131}Xe in the region between the $^2P_{3/2}$ and $^2P_{1/2}$ threshold markedly differ from those of the $I=0$ isotopes of Xe, the differences being caused by the hyperfine interaction. The experimental and theoretical study of these differences has provided a way to quantify the role of the nuclear spin in the photoionization of the rare-gas atoms and to characterize the process of hyperfine autoionization. It has also enabled us to derive the hyperfine structure of the Xe^+ ion.

In the modeling of the spectra by MQDT, excellent agreement between experimental spectra and spectra simulated by MQDT could be reached in a model in which the influence of the nuclear spin on the close-coupling eigenchannels was

neglected. The process of pure hyperfine autoionization, i.e., the autoionization process in which the ionic core transfers hyperfine energy to the electron to cause ionization, is found to be very efficient in the rare-gas atoms.

The hyperfine interaction is thus important in defining the hyperfine structure of the ion core and is propagated into the Rydberg spectrum by the angular momentum transformation. The autoionization dynamics (and the channel interactions) are entirely contained in the description of the eigenchannels, i.e., the eigenquantum defects which describe the electrostatic (orbit-orbit and exchange) interactions. Thus the dynamics of spin-orbit and hyperfine autoionization are both governed by the same interactions which, in our model, have nothing to do with the hyperfine interaction. The effect of the spin-orbit interaction on the dynamics are described by the spin-orbit structure of the ionic core on the one hand and by the different values of the eigenquantum defects of channels differing solely in their J values on the other hand. An essential element in the description of the details of the dynamics is given by the frame transformation matrix elements. It is therefore easy to explain why, at high J/F values, the branching ratios for autoionization into different channels approach a statistical distribution more closely than at low J/F values.

ACKNOWLEDGMENTS

We thank Dr. Ch. Jungen (Orsay) for useful discussions on the treatment, by MQDT, of the hyperfine structure in Rydberg states and for providing us with subroutines for solving the generalized eigenvalue problem. This work was supported financially by the Swiss National Science Foundation and the ETH Zürich.

[1] M. Quack, Mol. Phys. **34**, 477 (1977).
[2] J. Xie and R. N. Zare, J. Chem. Phys. **93**, 3033 (1990).
[3] R. Signorell and F. Merkt, Mol. Phys. **92**, 793 (1997).
[4] F. Merkt and H. Schmutz, J. Chem. Phys. **108**, 10033 (1998).
[5] U. Hollenstein, H. Palm, and F. Merkt, Rev. Sci. Instrum. **71**, 4023 (2000).
[6] K. T. Lu, Phys. Rev. A **4**, 579 (1971).
[7] M. J. Seaton, Rep. Prog. Phys. **46**, 167 (1983).
[8] U. Fano and A. R. P. Rau, *Atomic Collisions and Spectra* (Academic, Orlando, FL, 1986).
[9] Ch. Jungen, editor, *Molecular Applications of Quantum Defect Theory* (Institute of Physics Publishing, Bristol and Philadelphia, 1996).
[10] K. T. Lu, J. Q. Sun, and R. Beigang, Phys. Rev. A **37**, 2220 (1988).
[11] H. J. Wörner, U. Hollenstein, and F. Merkt, Phys. Rev. A **68**, 032510 (2003).
[12] A. Osterwalder, A. Wüest, F. Merkt, and Ch. Jungen, J. Chem. Phys. **121**, 11810 (2004).
[13] H. Lefebvre-Brion and R. W. Field, *The Spectra and Dynamics of Diatomic Molecules* (Elsevier, Amsterdam, 2004).
[14] G. Herzberg, *Molecular Spectra and Molecular Structure* (Krieger Publishing Company, Malabar, FL, 1966), Vol. III.
[15] H. Beutler, Z. Phys. **93**, 177 (1935).
[16] U. Fano, Phys. Rev. **124**, 1866 (1961).
[17] D. M. Lucas *et al.*, Phys. Rev. A **69**, 012711 (2004).
[18] A. M. Steane, Appl. Phys. B: Lasers Opt. **64**, 623 (1997).
[19] J. Geiger, Z. Phys. A **282**, 129 (1977).
[20] K. Maeda, K. Ueda, and K. Ito, J. Phys. B **26**, 1541 (1993).
[21] K. Yoshino and D. E. Freeman, J. Opt. Soc. Am. B **2**, 1268 (1985).
[22] A. Kortyna, M. R. Darrach, P. T. Howe, and A. Chutjian, J. Opt. Soc. Am. B **17**, 1934 (2000).
[23] W. R. Johnson, K. T. Cheng, K.-N. Huang, and M. Le Dourneuf, Phys. Rev. A **22**, 989 (1980).
[24] I. D. Petrov, V. L. Sukhoroukov, and H. Hotop, J. Phys. B **35**, 323 (2002).
[25] M. Hanif *et al.*, J. Phys. B **37**, 1987 (2004).
[26] S. M. Koeckhoven, W. J. Buma, and C. A. de Lange, Phys. Rev. A **49**, 3322 (1994).
[27] L. Wang and R. D. Knight, Phys. Rev. A **34**, 3902 (1986).
[28] R. D. Knight, Phys. Rev. A **34**, 3809 (1986).
[29] M. Ahmed, M. A. Zia, M. A. Baig, and B. Suleman, J. Phys. B **30**, 2155 (1998).
[30] W. Fischer, H. Hühnermann, G. Krömer, and H. J. Schäfer, Z. Phys. **270**, 113 (1974).
[31] G. D'Amico, G. Pesce, and A. Sasso, Hyperfine Interact. **127**, 121 (2000).
[32] F. Schneider, Ph.D. thesis, Freie Universität Berlin, 1985.
[33] F. Brandi, I. Velchev, W. Hogervorst, and W. Ubachs, Phys. Rev. A **64**, 032505 (2001).
[34] L. Broström, A. Kastberg, J. Lidberg, and S. R. Mannervik, Phys. Rev. A **53**, 109 (1996).
[35] K. Paduch and J. Bieron, J. Phys. B **33**, 303 (2000).
[36] U. Hollenstein, R. Seiler, and F. Merkt, J. Phys. B **36**, 893 (2003).
[37] *IODINESPEC*, simulation software, Toptica GmbH, 2004.
[38] H. Kopfermann, *Nuclear Moments* (Academic Press, New York, 1958).
[39] C. H. Greene and Ch. Jungen, Adv. At. Mol. Phys. **21**, 51 (1985).
[40] C. M. Lee, Phys. Rev. A **10**, 1598 (1974).
[41] E. U. Condon and G. H. Shortley, *The Theory of Atomic Spectra* (Cambridge University Press, London, 1953).
[42] K. Ueda, Phys. Rev. A **35**, 2484 (1987).
[43] R. Beigang, W. Makat, A. Timmermann, and P. J. West, Phys. Rev. Lett. **51**, 771 (1983).
[44] P. Labastie, M. C. Bordas, B. Tribollet, and M. Broyer, Phys. Rev. Lett. **52**, 1681 (1984).
[45] *IUPAC—Quantities, Units and Symbols in Physical Chemistry*, edited by I. Mills, T. Cvitaš, K. Homann, N. Kallay, and K. Kuchitsu, 2nd edition (Blackwell Scientific Publications, Oxford, 1993).